LETTER

https://doi.org/10.1038/s41586-018-0826-3

# Signatures of a jet cocoon in early spectra of a supernova associated with a γ-ray burst

L. Izzo[1]*, A. de Ugarte Postigo[1,2], K. Maeda[3], C. C. Thöne[1], D. A. Kann[1], M. Della Valle[1,4,5,6], A. Sagues Carracedo[7], M. J. Michałowski[8], P. Schady[9,10], S. Schmidl[11], J. Selsing[2,12,13], R. L. C. Starling[14], A. Suzuki[15], K. Bensch[1], J. Bolmer[9,16], S. Campana[17], Z. Cano[1], S. Covino[17], J. P. U. Fynbo[12,13], D. H. Hartmann[18], K. E. Heintz[12,13,19], J. Hjorth[2], J. Japelj[20], K. Kamiński[8], L. Kaper[20], C. Kouveliotou[21,22], M. Krużyński[8], T. Kwiatkowski[8], G. Leloudas[2,23], A. J. Levan[24], D. B. Malesani[2,12,13], T. Michałowski[8], S. Piranomonte[25], G. Pugliese[20], A. Rossi[26], R. Sánchez-Ramírez[27], S. Schulze[28], D. Steeghs[24], N. R. Tanvir[14], K. Ulaczyk[24], S. D. Vergani[29] & K. Wiersema[14,24]

**Long γ-ray bursts are associated with energetic, broad-lined, stripped-envelope supernovae[1,2] and as such mark the death of massive stars. The scarcity of such events nearby and the brightness of the γ-ray burst afterglow, which dominates the emission in the first few days after the burst, have so far prevented the study of the very early evolution of supernovae associated with γ-ray bursts[3]. In hydrogen-stripped supernovae that are not associated with γ-ray bursts, an excess of high-velocity (roughly 30,000 kilometres per second) material has been interpreted as a signature of a choked jet, which did not emerge from the progenitor star and instead deposited all of its energy in a thermal cocoon[4]. Here we report multi-epoch spectroscopic observations of the supernova SN 2017iuk, which is associated with the γ-ray burst GRB 171205A. Our spectra display features at extremely high expansion velocities (around 115,000 kilometres per second) within the first day after the burst[5,6]. Using spectral synthesis models developed for SN 2017iuk, we show that these features are characterized by chemical abundances that differ from those observed in the ejecta of SN 2017iuk at later times. We further show that the high-velocity features originate from the mildly relativistic hot cocoon that is generated by an ultra-relativistic jet within the γ-ray burst expanding and decelerating into the medium that surrounds the progenitor star[7,8]. This cocoon rapidly becomes transparent[9] and is outshone by the supernova emission, which starts to dominate the emission three days after the burst.**

On 2017 December 5, the Burst Alert Telescope (BAT) on-board the Neil Gehrels Swift Observatory triggered on a low-luminosity long γ-ray burst (GRB; isotropic luminosity of $L_{\mathrm{iso},\gamma} = 3.0 \times 10^{47}$ erg s$^{-1}$ in the 15–150-keV energy range, duration of $T_{90} = 190.0 \pm 35.0$ s)[10]. Its afterglow was promptly detected by the X-Ray Telescope (XRT) at a position coincident with the outskirts of a grand-design spiral galaxy (Fig. 1) at a redshift of $z = 0.0368$. We obtained spectroscopy of the afterglow 1.5 h after the GRB, which exhibited a bright continuum and typical nebular emission lines of Hα, [N II] (wavelength of $\lambda = 6{,}584$ Å) and the [S II] doublet ($\lambda = 6{,}717$ Å and $\lambda = 6{,}732$ Å) from the host galaxy[5]. The host is a massive system[11] ($\log(M_*/M_\odot) = 10.1 \pm 0.1$, where $M_*$ is the stellar mass and $M_\odot$ is the solar mass), with a relatively high metallicity ($12 + \log(\mathrm{O/H}) = 8.41$). It is much more massive than typical GRB hosts, which are normally metal-poor, star-forming dwarf galaxies, particularly at low redshift[12].

The proximity of GRB 171205A motivated us to undertake multi-wavelength photometric and spectroscopic follow-up observations. The light curve exhibits unusual behaviour, with colour evolution of the optical and ultraviolet emission at very early phases, in contrast to the rapid decay observed in X-ray emission. A few minutes after the burst, a first light-curve bump emerged, characterizing the emission during the first two days, with fast evolution from ultraviolet to redder wavelengths (Fig. 1). After the second day, the luminosity of the underlying supernova (SN 2017iuk) started to increase, reaching its maximum $B$-band magnitude on 2017 December 16.4 UT, roughly 11.0 days after the discovery of the GRB. The absolute $B$ and $V$ magnitudes at peak ($M_B = -17.5 \pm 0.1$ mag, $M_V = -18.4 \pm 0.1$ mag), obtained by assuming a distance to the source of $D = 163$ Mpc, place SN 2017iuk at the faint end of the luminosity distribution of supernovae associated with GRBs[3].

We obtained spectroscopic observations at a nearly daily cadence (Fig. 2). Subtracting the contribution of the faint afterglow in the optical spectra (Methods) confirms the presence of the aforementioned additional emission component during the first three days after the burst. This component is already visible in the first spectrum, about 1.5 h after the GRB discovery, as an excess of flux at blue wavelengths, increasing towards the ultraviolet. The multi-frequency (near infrared to X-ray) spectral energy distributions at multiple epochs during the first two days are shown in Fig. 1. We model this component with a black body (Fig. 1; Methods), motivated by the detection of a thermal component with a temperature of $kT = 86^{+13}_{-9}$ eV ($T = 9.9^{+1.5}_{-1.0} \times 10^5$ K) and an emitting radius of $r_{\mathrm{BB}} = (1.5 \pm 0.1) \times 10^{12}$ cm in the very early Swift-XRT emission from about 150 s to 400 s after the GRB trigger[13] (Fig. 2), and by the observation of thermal components in other GRB-associated supernovae[14,15].

The spectrum obtained at day 0.975 shows broad absorption features, which we identify as Si II ($\lambda = 6{,}355$ Å) and the Ca II triplet (centred at rest-frame $\lambda = 8{,}498$ Å). The expansion velocities, obtained from the minimum of the corresponding broad absorption lines, have values

[1]Instituto de Astrofísica de Andalucía (IAA-CSIC), Granada, Spain. [2]DARK, Niels Bohr Institute, University of Copenaghen, Copenhagen, Denmark. [3]Department of Astronomy, Kyoto University, Kyoto, Japan. [4]INAF—Osservatorio Astronomico di Capodimonte, Napoli, Italy. [5]International Center for Relativistic Astrophysics Network, Pescara, Italy. [6]LAPTh, Université de Savoie, CNRS, Annecy-le-Vieux, France. [7]The Oskar Klein Centre, Physics Department, Stockholm University, Stockholm, Sweden. [8]Astronomical Observatory Institute, Faculty of Physics, Adam Mickiewicz University, Poznań, Poland. [9]Max-Planck-Institut für Extraterrestrische Physik, Garching, Germany. [10]Department of Physics, University of Bath, Bath, UK. [11]Thüringer Landessternwarte Tautenburg, Tautenburg, Germany. [12]The Cosmic Dawn Center (DAWN), Niels Bohr Institute, University of Copenhagen, Copenhagen Ø, Denmark. [13]The Cosmic Dawn Center (DAWN), DTU-Space, Technical University of Denmark, Kongens Lyngby, Denmark. [14]Department of Physics and Astronomy, University of Leicester, Leicester, UK. [15]Division of Theoretical Astronomy, National Astronomical Observatory of Japan, National Institutes of Natural Sciences, Tokyo, Japan. [16]European Southern Observatory, Vitacura, Chile. [17]INAF—Osservatorio Astronomico di Brera, Merate, Italy. [18]Department of Physics and Astronomy, Clemson University, Clemson, SC, USA. [19]Centre for Astrophysics and Cosmology, Science Institute, University of Iceland, Reykjavik, Iceland. [20]Astronomical Institute Anton Pannekoek, University of Amsterdam, Amsterdam, The Netherlands. [21]Department of Physics, The George Washington University, Washington, DC, USA. [22]Astronomy, Physics and Statistics Institute of Sciences (APSIS), The George Washington University, Washington, DC, USA. [23]DTU Space, National Space Institute, Technical University of Denmark, Kongens Lyngby, Denmark. [24]Department of Physics, University of Warwick, Coventry, UK. [25]INAF—Osservatorio Astronomico di Roma, Monte Porzio Catone, Italy. [26]INAF—Osservatorio di Astrofisica e Scienza dello Spazio di Bologna, Bologna, Italy. [27]INAF—Istituto di Astrofisica e Planetologia Spaziali, Roma, Italy. [28]Department of Particle Physics and Astrophysics, Weizmann Institute of Science, Rehovot, Israel. [29]GEPI, Observatoire de Paris, PSL University, CNRS, Meudon, France. *e-mail: izzo@iaa.es

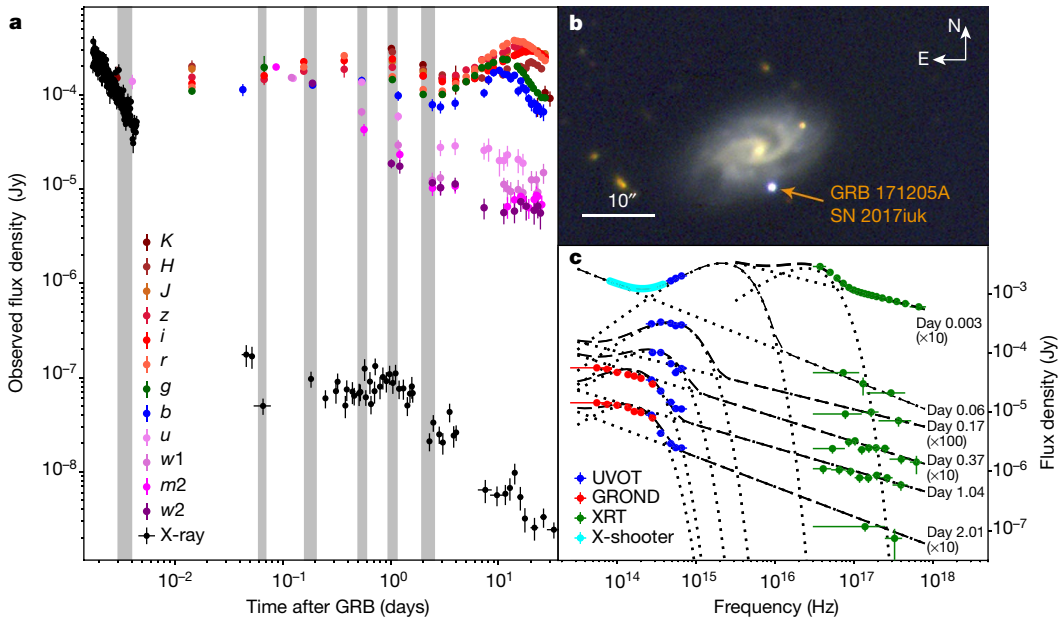


**Fig. 1 | Multi-wavelength evolution of the GRB 171205A/SN 2017iuk emission. a**, Multi-wavelength light curve of the optical transient following GRB 171205A. During the first three days, the optical, ultraviolet and near-infrared emission is dominated by a spectrally evolving bump. Beyond day 3, a component from a classical broad-lined type Ic supernova (SN 2017iuk) emerges. Grey regions correspond to the epochs of our analysis of the multi-frequency spectral energy distribution. **b**, True-colour (*gri*) image of GRB 171205A/SN 2017iuk and its spiral host galaxy, obtained with OSIRIS at the 10.4-m Gran Telescopio Canarias. **c**, The best-fit results using one or two black bodies plus a power-law spectral model for the six spectral energy distributions marked by grey shading in **a**, obtained with Swift for the ultraviolet (UVOT) and X-ray (XRT) emission and with ground telescopes (GROND and X-shooter). Dotted curves represent the black-body and the power-law spectral models; dashed curves represent the combination of the two models for each epoch. All error bars represent 1 s.d.

of about 115,000 km s$^{-1}$ (Fig. 3), with a full-width at half-maximum for the Ca II feature of around 35,000 km s$^{-1}$. These features become more prominent in the spectrum taken on the second day and show rapid evolution in their profiles. From these profiles we derive velocities of 105,000 km s$^{-1}$ for Ca II and 75,000 km s$^{-1}$ for Si II, which hint at the emergence of SN 2017iuk[6] associated with this GRB. The measured expansion velocities are greater than the fastest velocities ever observed in any known type of supernova: velocities up to roughly 40,000–50,000 km s$^{-1}$ are observed a few days after the burst in most supernovae associated with GRBs[1,2,16–18]. These velocities decline rapidly so that at peak the expansion velocity is normally[19] about 20,000–25,000 km s$^{-1}$. Therefore, the non-detection of absorption lines at very high velocities in all other GRB-associated supernovae may be the result of not having obtained spectroscopic observations at the very early stages of these events. From day 9.95 onwards, additional features become apparent: the C II ($\lambda = 6{,}580$ Å) line and

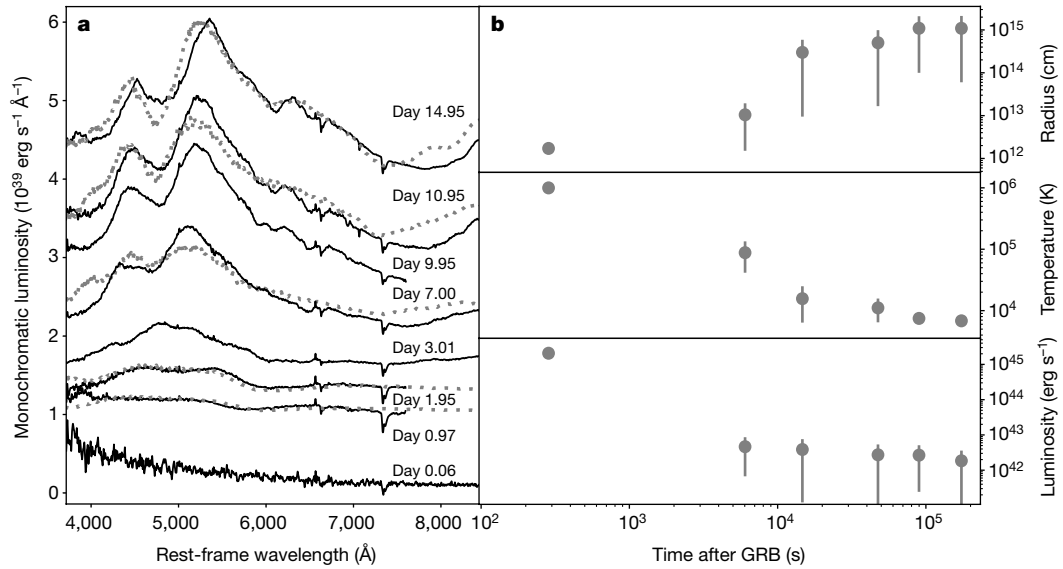


**Fig. 2 | Optical and X-ray spectral modelling of the early emission of SN 2017iuk. a**, The spectral evolution of SN 2017iuk during the first 15 days after the GRB. All spectra are shown as black curves, offset for clarity, and have been de-reddened for Galactic extinction. The contribution of the GRB afterglow has been subtracted as well. The simulated emission obtained from our synthesis model for some selected spectra are shown as grey dotted curves. For the spectral simulation at day 0.957, an arbitrary constant was applied to match the observed spectra, keeping in mind the uncertainty in the continuum of the afterglow component. **b**, Evolution of the black-body model parameters (radius, temperature and luminosity) as a function of time since the GRB detection. All error bars represent 1 s.d.

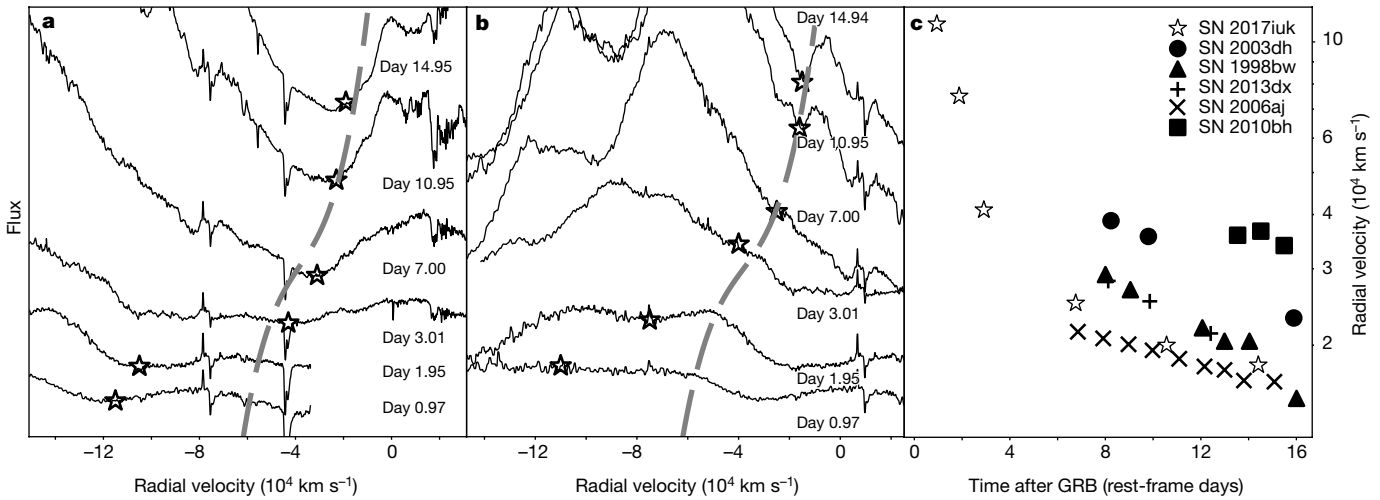


**Fig. 3 | Evolution of the ejecta velocities. a**, Temporal evolution of the Ca II near-infrared triplet, centred at a wavelength of 8,498 Å. Stars represent the values estimated for the expansion velocities at each spectral epoch. The dashed grey curve represents the model photospheric velocity obtained with TARDIS. **b**, Same as **a**, but for the Si II ($\lambda = 6{,}355$ Å) absorption line. **c**, Velocity variation estimated from the absorption line of Si II ($\lambda = 6{,}355$ Å) in the SN 2017iuk spectra up to day 14 (stars) and for the GRB-associated supernovae (other symbols; see legend) GRB 980425/SN 1998bw[1], GRB 030329/SN 2003dh[2], GRB 060218/SN 2006aj[17], GRB 100316D/SN 2010dh[16] and GRB 130427A/SN 2013dx[18].

Fe II multiplets (27, 37 and 38) are observed at the same blueshifted velocity of Si II ($\lambda = 6{,}355$ Å). On day 21.027 we see the emergence of another broad absorption line in the near-infrared, probably due to He I ($\lambda = 10{,}830$ Å).

The intense spectral coverage in the early phases of SN 2017iuk shows that a large amount of high-velocity material is required to reproduce the observed features and their evolution. The emission of GRB-associated supernovae is usually reproduced by using spectral synthesis models that adopt the CO138 model[20,21] but introducing a flat density distribution at high velocities. This is different from the behaviour of a canonical spherically symmetric supernova-explosion model, in which the density gradient steepens towards the outer layers[22]. In the case of SN 2017iuk, we developed spectral synthesis models that reproduce the high-velocity components and their evolution, assuming (i) a single power-law density distribution $\rho \propto v^{\alpha}$, where $v$ is the velocity and the index $\alpha \approx -6$, and (ii) a stratified compositional structure, whereby the relative fractions of different characteristic burning products are allowed to vary to take into account the hydrodynamical mixing in the explosion. The resulting simulated spectra match the observed spectral sequence very well from day 0.975 to day 14.936 (Fig. 2). Our model is also able to reproduce the high-velocity Si and Ca absorption features located in the region outside the photosphere, which on day 0.975 and day 1.947 are expanding at 59,000 km s$^{-1}$ and 53,000 km s$^{-1}$, respectively (Fig. 3). For the component above 55,000 km s$^{-1}$, where the enhancement of Fe-peak elements is seen, we find an ejected mass of $M = 0.13 M_{\odot}$ and a total kinetic energy of $E_{\rm kin} = 1.1 \times 10^{52}$ erg. Using the Ni-radioactive-heating spherically symmetric model[23] applied to the bolometric light curve of the supernova, we estimate the total mass ejected by the supernova and its Ni mass to be $M_{\rm ej} = (4.9 \pm 0.9) M_{\odot}$ and $M_{\rm Ni} = (0.18 \pm 0.01) M_{\odot}$, respectively. The total kinetic energy of the supernova is $E_{\rm kin} = (2.4 \pm 0.9) \times 10^{52}$ erg, in line with the average value inferred for other GRB-associated supernovae[3]. However, the presence of a jet implies a deviation from the spherical symmetry, so the full light curve and spectral evolution up to the nebular phases need to be modelled to accurately evaluate the ejecta mass and kinetic energy; the above results will serve as a reference for this analysis.

According to our spectral synthesis simulations (Methods), the chemical composition of the high-velocity material is different from that at lower velocities inferred for SN 2017iuk using later (from day 7) spectra. However, it is qualitatively consistent with the composition predicted by substantial mixing of the explosive material induced by the jet in models of typical GRB-associated supernovae[24,25]. We generally observe an increasing abundance of Ca, Ti, Cr and $^{56}$Ni towards lower velocities, whereas at the highest velocity there is evidence of nearly pure $^{56}$Ni and other Fe-peak elements, characterized by a more extreme abundance than the one typically inferred from non-relativistic simulations of jet-driven explosions (Fig. 4). These metal-rich blobs are created by the injection of the jet over a time span longer than the timescale of the shock or jet breakout. The abundances derived from absorption lines in high-velocity features match those expected in a scenario in which the GRB jet is responsible for a considerable fraction of the material in the line-forming regions.

These high-velocity features and their peculiar chemical composition are responsible for the blue emission superimposed on the evolution of the GRB afterglow, which is observed only in the first hours after the burst (Fig. 1). The flattening in the ejecta density structure is due to the presence of additional material at high velocities, which in turn implies energy input from the central engine on a timescale longer than the shock-wave breakout time of a typical[26] Wolf–Rayet star[27] (about 10 s). We interpret this fact as a signature of a hot cocoon generated as the jet emerges from the progenitor system[9]: as the jet breaks out, the inner material transported by the jet interacts with the external layers and the medium surrounding the progenitor star[7,8,28], spreading sideways and giving rise to the observed thermal emission[29].

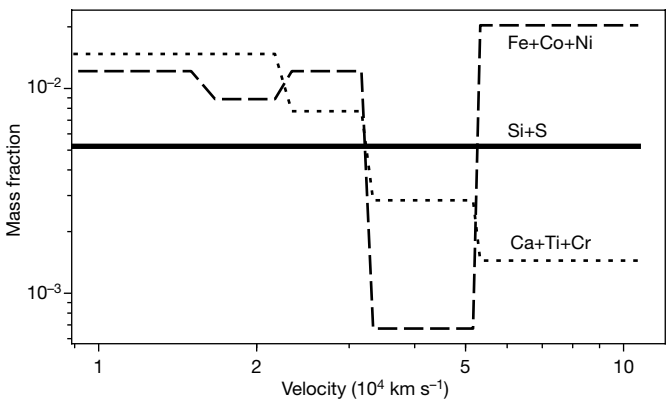


**Fig. 4 | Chemical composition of the supernova ejecta.** The plot shows the angle-averaged compositional abundance structure of the SN 2017iuk ejecta that is used in our spectral synthesis model. At very high velocity we observe an increase in the abundance of Fe and Ni, which is expected when the GRB jet injects metal-rich 'blobs' over a timescale longer than the typical shock or jet breakout.

The density and temperature of the hot cocoon material rapidly decrease with time. This enables a deeper and deeper view into the outflow, which explains the observed deceleration of the spectral features from mildly relativistic to sub-relativistic velocities, and the evolution of the emission excess observed at early epochs. This observation is also consistent with the expected luminosity evolution of the expanding and cooling cocoon[29] assuming an ejecta mass of $1.1 \times 10^{-3} M_{\odot}$ above 100,000 km $s^{-1}$. In addition, hydrodynamic simulations[30] of the emission from a hot cocoon reproduce the luminosity and temperature evolution observed at X-ray wavelengths in the early thermal component of GRB 171205A. The X-ray emission resembles the afterglow behaviour (albeit dimmer) observed in cosmological GRBs (Fig. 1). This suggests that the jet successfully drilled through the progenitor star, after depositing a considerable fraction of its energy into the cocoon (about $10^{52}$ erg). Consequently, only a small fraction of energy (about $10^{49}$ erg) was observed at $\gamma$-ray wavelengths. The explosion energy in low-luminosity GRBs associated with supernovae need not be lower than that in other, more energetic cosmological GRBs, but the final interaction of the emerging jet with the external envelope of the progenitor, which generates the cocoon emission, is responsible for lowering the energetic output of the event at $\gamma$-ray wavelengths.

## Online content

Any methods, additional references, Nature Research reporting summaries, source data, statements of data availability and associated accession codes are available at https://doi.org/10.1038/s41586-018-0826-3.

Received: 5 July 2018; Accepted: 15 November 2018;
Published online 16 January 2019.

1. Galama, T. J. et al. An unusual supernova in the error box of the $\gamma$-ray burst of 25 April 1998. *Nature* **395**, 670–672 (1998).
2. Hjorth, J. et al. A very energetic supernova associated with the $\gamma$-ray burst of 29 March 2003. *Nature* **423**, 847–850 (2003).
3. Cano, Z., Wang, S.-Q., Dai, Z.-G. & Wu, X.-F. The observer's guide to the gamma-ray burst supernova connection. *Adv. Astron.* **2017**, 8929054 (2017).
4. Piran, T., Nakar, E., Mazzali, P. & Pian, E. Relativistic jets in core collapse supernovae. Preprint at https://arxiv.org/abs/1704.08298 (2017).
5. Izzo, L. et al. GRB 171205A: VLT/X-shooter optical counterpart and spectroscopic observations. *GCN Circ.* 22180 (2017).
6. de Ugarte Postigo, A. et al. GRB 171205A: detection of the emerging SN. *GCN Circ.* 22204 (2017).
7. Bromberg, O., Nakar, E., Piran, T. & Sari, R. The propagation of relativistic jets in external media. *Astrophys. J.* **740**, 100 (2011).
8. Harrison, R., Gottlieb, O. & Nakar, E. Numerically calibrated model for propagation of a relativistic unmagnetized jet in dense media. *Mon. Not. R. Astron. Soc.* **477**, 2128–2140 (2018).
9. Ramirez-Ruiz, E., Celotti, A. & Rees, M. J. Events in the life of a cocoon surrounding a light, collapsar jet. *Mon. Not. R. Astron. Soc.* **337**, 1349–1356 (2002).
10. Barthelmy, S. D. et al. GRB 171205A: Swift-BAT refined analysis. *GCN Circ.* 22184 (2017).
11. Perley, D. A. & Taggart, K. GRB 171205A: host galaxy photometric properties. *GCN Circ.* 22194 (2017).
12. Vergani, S. et al. Are long gamma-ray bursts biased tracers of star formation? Clues from the host galaxies of the Swift/BAT6 complete sample of LGRBs. I. Stellar mass at $z \leq 1$. *Astron. Astrophys.* **581**, A102 (2015).
13. Campana, S. et al. Possible blackbody component in the X-ray spectrum of GRB171205A. *GCN Circ.* 22191 (2017).
14. Campana, S. et al. The association of GRB 060218 with a supernova and the evolution of the shock wave. *Nature* **442**, 1008–1010 (2006).
15. Starling, R. L. C., Page, K., Pe'er, A., Beardmore, A. & Osborne, J. P. A search for thermal X-ray signatures in gamma-ray bursts – I. Swift bursts with optical supernovae. *Mon. Not. R. Astron. Soc.* **427**, 2950–2964 (2012).
16. Bufano, F. et al. The highly energetic expansion of SN 2010bh associated with GRB 100316D. *Astrophys. J.* **753**, 67 (2012).
17. Modjaz, M. et al. Early-time photometry and spectroscopy of the fast evolving SN 2006aj associated with GRB 060218. *Astrophys. J.* **645**, L21–L24 (2006).
18. Xu, D. et al. Discovery of the broad-lined type Ic SN 2013cq associated with the very energetic GRB 130427A. *Astrophys. J.* **776**, 98 (2013).
19. Modjaz, M., Liu, Y. Q., Bianco, F. B. & Graur, O. The spectral SN-GRB connection: systematic spectral comparisons between type Ic supernovae and broad-lined type Ic supernovae with and without gamma-ray bursts. *Astrophys. J.* **832**, 108 (2016).
20. Iwamoto, K. et al. A hypernova model for the supernova associated with the $\gamma$-ray burst of 25 April 1998. *Nature* **395**, 672–674 (1998).
21. Nakamura, T. et al. Explosive nucleosynthesis in hypernovae. *Astrophys. J.* **555**, 880–899 (2001).
22. Matzner, C. D. & McKee, C. F. The expulsion of stellar envelopes in core-collapse supernovae. *Astrophys. J.* **510**, 379–403 (1999).
23. Arnett, W. D. Type I supernovae. I – analytic solutions for the early part of the light curve. *Astrophys. J.* **253**, 785–797 (1982).
24. Maeda, K. et al. Explosive nucleosynthesis in aspherical hypernova explosions and late-time spectra of SN1998bw. *Astrophys. J.* **565**, 405–412 (2002).
25. Maeda, K. & Nomoto, K. Bipolar supernova explosions: nucleosynthesis and implications for abundances in extremely metal-poor stars. *Astrophys. J.* **598**, 1163–1200 (2003).
26. Yoon, S.-C. & Langer, N. Evolution of rapidly rotating metal-poor massive stars towards gamma-ray bursts. *Astron. Astrophys.* **443**, 643–648 (2005).
27. Moriya, T. J., Sanyal, D. & Langer, N. Extended supernova shock breakout signals from inflated stellar envelopes. *Astron. Astrophys.* **575**, L10 (2015).
28. Suzuki, A. & Maeda, K. Broad-band emission properties of central engine-powered supernova ejecta interacting with a circumstellar medium. *Mon. Not. R. Astron. Soc.* **478**, 110–125 (2018).
29. Nakar, E. & Piran, T. The observable signatures of GRB cocoons. *Astrophys. J.* **834**, 28 (2017).
30. De Colle, F., Lu, W., Kumar, P., Ramirez-Ruiz, E. & Smoot, G. Thermal and non-thermal emission from the cocoon of a gamma-ray burst jet. *Mon. Not. R. Astron. Soc.* **478**, 4553–4564 (2018).

**Acknowledgements** We acknowledge A. S. Esposito for the rendering of the figures presented in this work. L.I. acknowledges support from funding associated with Juan de la Cierva Incorporacion fellowship IJCI-2016-30940. L.I., A.d.U.P., C.C.T. and D.A.K. acknowledge support from the Spanish research project AYA2017-89384-P. A.d.U.P. acknowledges support from funding associated with Ramón y Cajal fellowship RyC-2012-09975. C.C.T. acknowledges support from funding associated with Ramón y Cajal fellowship RyC-2012-09984. D.A.K. acknowledges support from funding associated with Juan de la Cierva Incorporacion fellowship IJCI-2015-26153. K.M. acknowledges support from JSPS Kakenhi grants (18H05223, 18H04585 and 17H02864). S. Schmidl acknowledges support from grant DFG Klose 766/16-3 and discussions with S. Klose. R.L.C.S. acknowledges funding from STFC. M.J.M. acknowledges the support of the National Science Centre, Poland, through POLONEZ grant 2015/19/P/ST9/04010; this project has received funding from the European Union's Horizon 2020 research and innovation programme under Marie Skłodowska-Curie grant agreement number 665778. R.S.-R. acknowledges support from ASI (Italian Space Agency) through contract number 2015-046-R.0 and from the European Union's Horizon 2020 programme under the AHEAD project (grant agreement number 654215). The Cosmic Dawn Center is funded by the DNRF. J.H. was supported by a VILLUM FONDEN Investigator grant (project number 16599). G.L. was supported by a research grant from VILLUM FONDEN (project number 19054). K.E.H. acknowledges support by a Project Grant (162948–051) from The Icelandic Research fund. J.J. and L.K. acknowledge support from NOVA and NWO-FAPESP grant for advanced instrumentation in astronomy.

**Author contributions** L.I., K.M., A.d.U.P., D.A.K., M.D.V., P.S. and C.C.T. wrote the manuscript. L.I., D.A.K. and A.d.U.P. coordinated the follow-up efforts. L.I., main coordination, X-ray and optical data reduction, spectral analysis and SED interpretation. A.d.U.P., GTC spectroscopic data reduction and analysis, discovery of the emerging supernova and the high-velocity components. K.M. and A.S., spectral synthesis modelling and interpretation. A.S.C., supernova data analysis and interpretation. N.R.T., C.C.T. and D.A.K., principal investigators of the VLT and GTC afterglow/GRB-associated supernova proposals with which all spectra were obtained. M.J.M., T.M., K.K., T.K. and M.K., planning and analysis of the RBT/PST2 observations. J.S. and J.J., VLT data reduction and analysis. K.E.H. and D.B.M. led and planned the NOT observations. P.S. and S. Schmidl contributed to UVOT and GROND data analysis and interpretation. R.L.C.S. contributed to X-ray data analysis and interpretation. D.S., K.U. and R.L.C.S. planned and analysed the GOTO observations. L.I., A.d.U.P., D.A.K., C.C.T., M.D.V., K.B., J.B., S. Campana, Z.C., S. Covino, J.P.U.F., D.H.H., K.E.H., J.H., L.K., C.K., G.L., A.J.L., D.B.M., G.P., S.P., A.R., R.S.-R., S. Schulze, D.S., N.R.T., S.D.V. and K.W. contributed to observation strategy and planning for X-shooter observations. All authors contributed to the discussion and presentation of the results and reviewed the manuscript.

**Competing interests** The authors declare no competing interests.

**Additional information**
**Extended data** is available for this paper at https://doi.org/10.1038/s41586-018-0826-3.
**Reprints and permissions information** is available at http://www.nature.com/reprints.
**Correspondence and requests for materials** should be addressed to L.I.
**Publisher's note:** Springer Nature remains neutral with regard to jurisdictional claims in published maps and institutional affiliations.

## METHODS

**Photometry.** After the discovery of GRB 171205A by the Neil Gehrels Swift Observatory satellite mission[31], we promptly started a monitoring campaign using several telescopes distributed worldwide. We obtained optical and near-infrared (NIR) observations in the $g'r'i'z'JHK$ filters with the Gamma-Ray Burst Optical and Near-Infrared Detector (GROND)[32] mounted on the MPG 2.2-m telescope at the European Southern Observatory (ESO) La Silla Observatory, Chile. $V$ and $R_C$ imaging was obtained with StanCam mounted at the 2.5-m Nordic Optical Telescope (NOT), Spain. We also obtained $BVRI$ imaging using the 1.5-m telescope located at the Observatorio de Sierra Nevada (OSN), Spain, and $R_C$ imaging at smaller remote telescopes (http://itelescope.net; http://www.astrocampania.it). Additional data were obtained with the Gravitational-Wave Optical Transient Observer (GOTO; https://goto-observatory.org), an array of wide-field ($D = 40$ cm $f/2.5$) optical telescopes on a common mount, stationed at La Palma Observatory, Spain. Observations were carried out during commissioning of the facility, when three telescopes were active. We also obtained $BVR_CI_C$ photometry with the Roman Baranowski Telescope/Poznań Spectroscopic Telescope 2 (RBT/PST2; http://www.astro.amu.edu.pl/GATS), a 0.7-m robotic telescope located at Winer Observatory, USA. Photometry of the object was performed with an aperture radius of 2 arcsec and aperture correction applied. The host-galaxy contribution was estimated by using an aperture of the same size but centred on different parts of the galaxy with similar brightness profiles to the source location. For GOTO data, the magnitudes are Baader $R$ and $G$, which were calibrated by cross-matching with the AAVSO Photometric All-Sky Survey Data Release 9 (APASS DR9), using $r$ (AB) and $V$ (Vega) magnitudes, and photometry was performed on the object with an aperture radius of three pixels and aperture correction applied.

The entire dataset of our photometric follow-up is available at https://osf.io/apq3d/. The values are corrected neither for Galactic extinction along the line of sight of $E(B-V) = 0.05$ mag nor for the extinction intrinsic to the host of $E(B-V)_{\rm int} = 0.02$ mag (see below).

**Spectroscopy.** We first observed the bright ($r' \approx 16.0$) afterglow just 1.5 h after the GRB discovery with X-shooter at the ESO Very Large Telescope (VLT). We identified typical nebular emission lines of H$\alpha$, N II $\lambda$6584 and S II $\lambda\lambda$6717/32 at a common redshift of $z = 0.0368$, which confirmed the association of GRB 171205A with the galaxy 6dFGS gJ110939.7−123512.

In parallel, we activated our GRB/supernova programmes at the Gran Telescopio Canarias (GTC) with OSIRIS. The first spectrum with GTC/OSIRIS was obtained 0.975 days after the GRB, followed by observations with an almost daily cadence and complemented by additional X-shooter observations. All spectroscopic observations are presented in Extended Data Table 1.

**High-energy observations.** We reduced and analysed Swift X-ray and Ultraviolet/Optical Telescope (UVOT)[33] data of GRB 171205A. The XRT data were obtained from the public Swift data archive and then reduced with the standard HEASOFT *xrtpipeline* tool (version 6.22.1), after which we extracted time-resolved spectra at six different epochs using *xselect* (Extended Data Table 2). Ancillary response files were built using the *xrtmkarf* tool, using exposure maps for each single observation epoch.

Pipeline-processed UV and optical sky images taken with UVOT were downloaded from the UK Swift Science Data Centre. Individual exposures at any given observing epoch were combined for each of the seven UVOT filters ($v$, $b$, $u$, $uvw1$, $uvm2$, $uvw2$ and white). UVOT photometry was obtained following the standard procedure[34] using a 3-arcsec-radius source-extraction region centred at the position of the GRB/supernova. An aperture correction was applied to remain compatible with the effective-area calibrations, which are based on 5-arcsec aperture photometry[34]. The background was estimated using a 5-arcsec-radius extraction region located at a similar distance from the host galaxy centre as the GRB. In the absence of pre-explosion host-galaxy UVOT template images, we considered our choice of a background region the best way to remove the contamination by host-galaxy light from our GRB/supernova photometry.

**Data analysis of the initial two days.** According to the standard GRB afterglow scenario[35], the spectral energy distribution (SED) is the result of synchrotron emission from shock-accelerated electrons, which is best modelled with a power-law (possibly a broken power-law) from X-ray to optical frequencies. This implies that extinction-corrected colour indices are generally constant during the entire duration of the GRB afterglow[36]. At very early epochs, the optical data for the optical counterpart of GRB 171205A do not show the typical decay observed in GRB afterglows, a behaviour that is instead observed in the UVOT $uvw2$, $uvm2$ and $uvw1$ filters. A similar trend is observed for the other UVOT filters ($u$, $b$ and $v$), but starting at later times. This is similar to the behaviour observed in GRB 060218[14], suggesting the presence of an additional component in the early light-curve evolution. Evidence for cooling thermal emission peaking at UV and optical wavelengths can be found in the colour-index evolution. We use UVOT data to build colour evolution curves of $u-b$, $b-v$, $uvw1-u$ and $uvw2-uvw1$ (Extended Data Fig. 1). Our results show a variation during the first day of the GRB emission for all colour indices except $uvw2-uvw1$. Late-time variations of the $u-b$ colour index are due to the emerging supernova component. For synchrotron emission, a variation in the optical colours is possible only because of the passage of the synchrotron break frequency at optical frequencies[37]. In our case, millimetre observations and spectral indices derived from X-ray spectra suggest that the cooling break frequency lies at longer wavelengths[11], ruling out this option. Furthermore, the late-time behaviour is dominated by the supernova emission: we observe a steep rise at optical wavelengths while UV colours remain almost constant owing to the effect of line blanketing and residual emission from the host galaxy (this is visible also at late epochs in the light curve in Fig. 1).

To further investigate the origin of the first emission bump and the observed colour index variations we constructed six SEDs using our own dataset for the NIR–near-UV range and Swift XRT data for the X-ray part (Extended Data Fig. 2). The SEDs are computed at mean epochs of $T_{\rm SED1} = 0.003$ days, $T_{\rm SED2} = 0.06$ days, $T_{\rm SED3} = 0.17$ days, $T_{\rm SED4} = 0.55$ days, $T_{\rm SED5} = 0.97$ days and $T_{\rm SED6} = 1.95$ days from the GRB trigger. The last two SEDs correspond to the second and third epochs of our spectral dataset. We fit the SEDs using the XSPEC software[38]. We follow the general fitting procedure[39], where the absorption component for the Galactic interstellar extinction is[40,41] $E(B-V) = 0.05$ mag and the column density $N({\rm H\,I}) = 5.89 \times 10^{20}$ cm$^{-2}$, obtained using the Cardelli extinction curve[42]. A second absorption component corrects for the host-galaxy extinction by dust scattering using the Milky Way ($R_V = 3.08$) template[43]. We estimate this intrinsic $E(B-V)$ value from the observed Na I $\lambda$5890 line in the X-shooter spectra. We use the spectra from day 7 and day 21 to measure its equivalent width and obtain an extinction of $E(B-V)_{\rm int} = 0.02 \pm 0.01$ mag according to the Poznanski relation[44]. Moreover, from an X-shooter spectrum at day 56 we measure H$\alpha$/H$\beta = 2.89$, corresponding to $E(B-V)_{\rm int} = 0.01$ mag, in agreement with Na I measurements, and assuming an electron temperature of $T_{\rm e} = 10^4$ K and density of $n_{\rm e} = 10^2$ cm$^{-3}$ for case B recombination[45]. For the Galactic and host X-ray absorption components, we used the Tübingen–Boulder interstellar medium absorption model[46]. To estimate the intrinsic X-ray column density $N_{\rm H,int}$, including the effects of metallicity, we fit late-time XRT data in the time interval $(1.5 \times 10^4, 3.0 \times 10^6)$ s, obtaining $N_{\rm H,int} = 9^{+6}_{-5} \times 10^{20}$ cm$^{-2}$. In our SED fits, we fix the $N_{\rm H,int}$ value to that determined from late-time X-rays.

Our analysis shows that the broadband SED cannot be fitted with a single power-law function. At optical–UV frequencies we find a clear excess above the extrapolated power-law best-fit function to the X-ray data alone (Extended Data Table 2). We exclude the passage of the synchrotron break frequency at optical wavelengths as the origin of the observed colour index variation. In this case our NIR–near-UV data should follow a power-law function with spectral index $\beta_{\rm X} + 0.5$, but with a lower flux than the one observed. We model this excess as a black body, motivated by the presence of a thermal component in the XRT windowed-timing spectra from around 150 s to 400 s after the GRB trigger[13]. We fitted the X-rays in the interval ($T_0 + 185$ s, $T_0 + 385$ s), taking the $N_{\rm H,int}$ value determined at later times (see above). We confirm the presence of an additional thermal component with an observed temperature of $kT = 86^{+13}_{-9}$ eV ($T = 9.9^{+1.5}_{-1.0} \times 10^5$ K) and an emitting radius of $r_{\rm BB} \approx 10^{12}$ cm (Extended Data Tables 2, 3).

The paucity of data (Extended Data Table 2) does not allow for a better constraint on the spectral model parameters for the SEDs at day 0.17 and day 0.55, leading to relatively large uncertainties for the black-body temperature and radius. Despite this we observe an evolution of the thermal component with time. The temperature decreases from about 200,000 K to 5,000 K from day 0.06 to day 2, while the radius of the emitter increases from $2 \times 10^{12}$ cm to $10^{15}$ cm (Fig. 2).

**Evolution from day 2 onwards.** From day 2 onwards, the light curve at optical wavelengths becomes increasingly dominated by rising emission from the underlying supernova (SN 2017iuk). We fit the $BVR_CI_C$ light curves of SN 2017iuk with smoothed spline interpolation functions to determine the maximum of the supernova emission. SN 2017iuk reached maximum $B$-band magnitude on December 16.4 UT, 11.0 days after the GRB discovery (Extended Data Fig. 3). Applying K-correction, the absolute magnitudes at the peak are $M_B = -17.5 \pm 0.1$ mag and $M_V = -18.4 \pm 0.1$ mag. This suggests that SN 2017iuk is one of the faintest broad-lined supernovae connected to GRBs[3,47]. This is also visible in Extended Data Fig. 4, in which we compare the extinction-corrected absolute-magnitude light curve of SN 2017iuk with the emission of the two nearest GRB-associated supernovae, SN 1998bw and SN 2006aj[48,49]. The faintness of the supernova is consistent with the low luminosity of the GRB[50] and with the supernova luminosity peak at day 11[3].

We constructed a bolometric light curve of the supernova emission using our $uBVR_CI_CJH$ photometry to estimate the initial mass of Ni and the total ejecta mass of the supernova using the radioactive-heating model[23,51]. This model considers full trapping of $\gamma$-rays where the supernova is powered by the decay of Ni and Co into daughter products: the $\gamma$-rays produced in the decay interact with the supernova ejecta, thermalizing it and giving rise to the observed supernova emission. Assuming an optical opacity of $\kappa = 0.07$ cm$^2$ g$^{-1}$ and an

observed photospheric velocity at peak of $v_{phot} = 22{,}000$ km s$^{-1}$, we obtain a Ni mass of $M_{Ni} = (0.18 \pm 0.01)M_{\odot}$, a total mass ejected in the supernova of $M_{ej} = (5.4 \pm 1.4)M_{\odot}$ and a kinetic energy of $E_{kin} = (2.6 \pm 1.1) \times 10^{52}$ erg. More details on the formulation of the radioactive-heating model used in this analysis and the bolometric light curve construction method can be found elsewhere[52]. An important caveat of this model is in the assumption of spherical symmetry for the supernova ejecta. In the case of GRB 171205A/SN 2017iuk the jet/cocoon ejection was along the polar axis rather than being spherical, and so our model fits are likely to over-estimate the supernova ejected mass and its kinetic energy. Moreover, in the assumption of spherical symmetry, previous applications of the radioactive-heating scenario failed to estimate the luminosity in the nebular phase, in particular that of the [O I] $\lambda\lambda$6300/63 lines[53]. Consequently, modelling of the complete light curve and spectral evolution up to the nebular phase is needed to accurately estimate the ejecta parameters.

**Spectral analysis.** Optical spectra of GRB 171205A/SN 2017iuk were obtained at the VLT and GTC between day 0.06 and day 29.926 with an almost daily cadence (Extended Data Table 1). We first determined, and subtracted, the contribution of the GRB afterglow at optical wavelengths by extrapolating the observed X-ray emission, which in GRBs mostly tracks the evolution of the optical afterglow[54]. In the case of GRB 171205A, the X-ray afterglow is best modelled by a power-law function with spectral index $\beta = -0.85$. From standard fireball theory[37] we know that such a value is valid only for the part of the synchrotron spectrum between the peak of the synchrotron emission and the cooling break. Millimetric observations[55] indicate that the spectral peak is well beyond NIR wavelengths; hence, we can assume that the afterglow emission in the optical range is just the extension of the power law that we observe in X-rays. The result of this subtraction confirms the presence of an extra emission component during the first two days, in particular in the first spectrum obtained about 1.5 h after the GRB discovery, in which we observe an emission excess at blue wavelengths which extends and even increases into the UV (Extended Data Fig. 5). A possible absorption feature is also reported at around 3,700 Å, but the lack of additional data at bluer wavelengths prevents a more detailed analysis of its origin. Starting at day 0.975 we note the presence of broad spectral lines at very high recession velocities, typical of supernovae associated with GRBs. On day 0.975 we measure velocities of about 115,000 km s$^{-1}$ for Si II and the Ca II triplet centred at $\lambda$8498. These velocities rapidly decrease in the following days, reaching typical values observed for GRB-associated supernovae of around 20,000 km s$^{-1}$ at day 10.952.

From day 9.95 onwards we also detect C II $\lambda$6580, Fe II (multiplets 27, 37 and 38) and Mg II $\lambda$4481 at the same velocities as Ca II. At late epochs, the absorption velocities equally decline and reach values of about 15,000 km s$^{-1}$. In the spectrum of day 21.027 we observe a broad absorption feature possibly due to He I $\lambda$10830 at a velocity of 13,000 km s$^{-1}$ (Extended Data Fig. 6). If this feature is caused by He I then we should also detect the He I $\lambda$20580 line, but this region of our spectra is affected by telluric absorption features. Likewise, we cannot confirm the detection of any other He I line because the transitions at $\lambda\lambda$4471/5876/7065 would be blended with other broad systems in this part of the spectrum. This situation is similar to other broad-lined supernovae for which He detection has been claimed[56–58]. If we exclude He as the origin of this feature, then the most plausible alternative is Mg II $\lambda$10914 at about 15,000 km s$^{-1}$.

**The spectra from day 1 to day 15.** We constructed a model that aims to capture the overall behaviour in each of the spectra and their evolution with time, rather than providing detailed fits to every feature. For a specific density and abundance structure given as input parameters, we synthesize a model spectrum using Monte Carlo radiation-transfer simulations with the TARDIS (https://tardis.readthedocs.io/en/latest/) code[59]. TARDIS assumes a sharp photosphere with the luminosity and temperature as input parameters to the simulation, which are iteratively constrained through the spectral modelling. For the treatment of the micro-physics we adopt the following parameters: (1) nebular for ionization; (2) dilute local thermodynamic equilibrium (LTE) for excitation; (3) detailed Monte Carlo estimators for radiative rates; and (4) the 'macroatom' formalism for line-interaction type. The macroatom formalism represents the most complex form of line interactions, which is more advanced than the frequently adopted downward branching scheme. The code includes relativistic effects in the form of the Doppler shift to first order in $v/c$. In our case the second-order term would reach about 10% difference in wavelength, but this would not change our main conclusions. The most important limitations (due to simplicity) in our analysis could be a lack of full non-LTE and non-thermal effects. Although qualitatively we expect that (dilute) LTE provides a better approximation in earlier epochs, the spectral formation is intrinsically a non-LTE problem. The main feature in our spectral formation does not involve ions at high ionization potentials or transitions from high energy levels for which the non-thermal effects are definitely important[60]. However, this does not guarantee that we can totally ignore possible non-thermal effects. Nonetheless, such simplifications (neglecting non-LTE and non-thermal effects) are frequently adopted and result in well-tested models of the early-phases of the supernova spectral formation. Given these limitations, the abundance distribution that we derived (Fig. 4) should not be interpreted in a quantitative way.

Previous studies suggest that the density distribution at high velocities is flatter than the one predicted by the standard one-dimensional thermal bomb models. As an example, the model 'CO138E30', originally proposed[20,21] for SN 1998bw and frequently used in similar studies, has a power-law density index as a function of velocity of about $-6$ below 40,000 km s$^{-1}$ and about $-9$ at higher velocities. However, in case of SN 1997ef, an index of around $-4$ at and above 25,000 km s$^{-1}$ has been proposed[61]. A similar structure was considered for SN 2016jca (GRB 161219B) to reproduce the high-velocity absorption[62] observed in the Si II $\lambda$6355 line with roughly 42,000 km s$^{-1}$ in the spectrum of day 5.52. In this supernova, high-velocity material had been reported in the earlier spectrum of day 3.73, for which photospheric velocities of around 44,000 km s$^{-1}$ and a high abundance of Fe-peak elements in the ejecta were derived[62].

We analysed the density structure based on model CO138E30 as a first input model to our spectral synthesis simulations. To construct our reference density structure, the density and velocity scales are changed to agree with the estimate of the ejecta mass and kinetic energy obtained from the bolometric light-curve analysis in the previous section. In studying the spectrum formation with this model, we find a lack of a sufficient amount of material at high velocities to account for the high-velocity absorption features seen in all the phases examined here. This conclusion is not affected by the abundance distribution: the high-velocity absorptions are not formed even if we allow extensive mixing of the Fe-peak elements in the outermost layer. We further test a simple ejecta structure assuming a single power-law index of $-6$: there is not much improvement for the C + O core composition, but there is substantial change in the spectral features once this is coupled with the extensive mixing of the explosively synthesized elements to the level expected for homogeneous mixing[21]. In particular, the improvement in the first two days under the combination of these simple assumptions (a single power-law plus homogeneous mixing) is marked, and we hereafter take this density structure as our reference model.

The most plausible explanation for the origin of such high-velocity material is a long-lasting energy input from a central engine with the energy injection occurring on timescales substantially longer than the shock-wave breakout within the progenitor star (up to 10 s for a Wolf–Rayet progenitor), leading to a flat density structure[28]. The resulting density structure is well represented by a single power-law with index of around $-6$. From a theoretical point of view, this model represents the central-engine-driven explosion scenario (such as the collapsar model[63] or magnetar formation[64]) better than an instantaneous thermal bomb model such as CO138E30.

The above-mentioned ejecta model captures the basic feature of the theoretically motivated flat density structure and is coupled with another prediction from such a model: the extensive mixing of newly synthesized elements into the outer layers. However, the fits to the spectra at the later epochs are not satisfactory if a homogeneous abundance distribution is assumed. To identify important characteristics in the explosion mechanism, we further divide the ejecta structure into several zones and change the abundance distribution in the input models for the radiative-transfer simulations. The default abundance pattern is set to the typical mass fractions of a CO layer of a progenitor star with an initial mass of $M_{ZAMS} = 40M_{\odot}$ (C 0.01, Mg 0.05, Si 0.005 in mass fraction, with the remaining fraction associated with O) added to the half-solar abundance for Na, S and heavier elements up to Cu (Extended Data Table 4). Additional contributions are considered for (Si, S), (Ca, Ti, Cr) and (Fe, Co, Ni, $^{56}$Ni) to allow for mixing of the explosively synthesized elements into the outer layers, divided into three groups as shown by the parentheses, and the relative fractions of the elements in the same group are fixed and unchanged. The ratio S/Si in this additional contribution is fixed to 0.5; the ratios Ti/Ca and Cr/Ca are fixed to 0.2 and 0.66; and the ratios Fe/$^{56}$Ni, Co/$^{56}$Ni and Ni/$^{56}$Ni (where the numerator is the stable nuclei) are fixed to 0.2, 0.005 and 0.25, respectively. These ratios reflect typical theoretical predictions for each burning stage. Therefore, in each zone we have only three free parameters to describe the compositions (the mass fractions of Si/S, Ca/Ti/Cr and Fe/Co/Ni/$^{56}$Ni), which describe the hydrodynamical mixing of different burning zones. The same structure is used for the entire spectral sequence. Although the structure below the photosphere is not known and so the earlier phase modelling does not constrain the deeper part, the material at velocities above the photosphere can participate substantially in forming the absorption lines.

Figure 2 shows our reference model spectra thus obtained compared to the spectra of SN 2017iuk at the five reference epochs; the photospheric velocities in the model are shown in Fig. 3. The model luminosity and photospheric velocity are also given in Extended Data Table 3. The composition pattern is shown in Fig. 4, with detailed values given in Extended Data Table 4. The uncertainty in the derived composition structure is tested by changing the Fe-peak and Ca/Ti/Cr abundances at different layers, with a range of photospheric temperatures. We thereby conclude that the increasingly high abundance of Fe-peak elements at the highest velocity

is required to be consistent with the observed spectral sequence, whereas only modest enhancement of Ca/Ti/Cr compared to the Fe-peak elements is required. A similar analysis is done for the density in the outermost layer and outermost velocity, which confirms the need for substantial material up to about 110,000 km $s^{-1}$. The model contains a total ejecta mass of about $2.5M_{\odot}$ and a kinetic energy of $1.7 \times 10^{52}$ erg above 10,000 km $s^{-1}$. With this model, we also find an ejecta mass of $1.1 \times 10^{-3}M_{\odot}$ and a kinetic energy of $1.2 \times 10^{50}$ erg for the high-velocity component above 100,000 km $s^{-1}$. The flatter density structure reproduces the overall spectral evolution and the existence of the high-velocity absorption features observed in the earliest spectra at day 0.975 and day 1.947. (Fig. 2). The outermost velocity of the bulk ejecta material is constrained to be about 110,000 km $s^{-1}$; the lack of material below this velocity or the existence of material above this velocity should be visible through strong absorption.

The abundance distribution in our model has several interesting features, especially for the highest velocity range: (1) the strong absorption below about 4,500 Å at day 1.975 requires a large abundance of Fe-peak elements exceeding the homogeneous-mixing level above about 55,000 km $s^{-1}$; (2) the smaller abundance of Fe-peak elements between roughly 30,000 km $s^{-1}$ and 55,000 km $s^{-1}$ implies limited absorption below about 5,000 Å at later epochs; and (3) the presence of a modest overabundance of (Ca, Ti, Cr)-group elements at these high velocities, with the pre-supernova value unable to produce the high-velocity Ca II at day 1.975 but with a too high abundance producing too much absorption at later epochs. Below about 30,000 km $s^{-1}$, we see an increasing abundance of Fe-peak elements and of (Ca, Ti, Cr) to fit to the spectral evolution at day 7 onwards.

Although our ejecta model is dominated by the oxygen core material, the most abundant elements are not traced directly in SN 2017iuk. To reproduce the spectral sequence, we require high abundances of the explosive burning products such as the Fe-peak elements and Ca; under these conditions oxygen, carbon and magnesium, despite their large abundances, would not create strong lines[65]. In other words, we are not able to reproduce the spectral sequence of SN 2017iuk with the condition that these elements produce strong lines. In addition, our reference model has difficulty reproducing the low-velocity absorption in Ca II NIR at day 7 onwards: the model has a too strong emission contribution in the P-Cygni profile. This may indicate the importance of asymmetry in the ejecta. For example, if the highest-velocity material is pointing only towards an observer, the emission component would be suppressed in the later epochs when the outermost layer becomes transparent, whereas the presence of off-axis high-velocity material is assumed in the spectrum synthesis simulations under the spherical-symmetry assumption.

**Implications of the derived ejecta structure.** The characteristic composition structure that we inferred can be compared to the mass fractions expected in the homogeneous mixing of the explosively synthesized species for the CO138 model (Fig. 4). The overall composition structure is largely consistent with the mass fractions expected from the homogeneous mixing of explosive material within the whole ejecta. The heavier elements tend to increase towards lower velocities, suggesting that the mixing is not complete (although it is already substantial). However, in the highest-velocity (more than 55,000 km $s^{-1}$) material this is inverted: the mass fractions of $^{56}$Ni and stable Fe-peak elements are overabundant without enhancement of Ca/Ti/Cr. This analysis suggests that: (1) extensive mixing of the newly synthesized elements and pre-explosion progenitor compositions is required; (2) the degree of mixing is nearly at the level of homogeneous mixing but the layered structure is still kept; and (3) there is further inversion of more 'explosive' species in the outer and faster region. This characteristic behaviour may be similar to what has been suggested[62] for GRB 161219B/SN 2016jca to explain the spectrum 3.73 days after the GRB with a photospheric velocity of 44,000 km $s^{-1}$. Our first two spectra of GRB 171205A were taken much earlier and the photospheric velocities that we derived are higher; therefore, our analysis is more sensitive to the abundances in the outermost layer. Our study suggests that the existence of high-velocity Fe is directly visible as an absorption line at day 0.975 with a velocity of about 90,000 km $s^{-1}$ (Fig. 2).

In the case of GRB 161219B/ SN 2016jca, a jet-like explosion with the high-velocity 'Fe blob' pointing towards an observer had been suggested. A similar configuration may apply to SN 2017iuk. The jet-driven model 40A[25] predicts a mass fraction (in solar masses) of $X(^{56}\mathrm{Ni}) > 0.1$, $X(\mathrm{Ca}) \approx X(\mathrm{Ti}) \approx 10^{-3}$ and $X(\mathrm{Si}) \approx 10^{-4}$ at more than 20,000 km $s^{-1}$ along the jet axis. The mass fractions averaged over the whole ejecta, including the non-jet direction, are $X(^{56}\mathrm{Ni}) \approx X(\mathrm{Si}) \approx 0.01$–$0.1$ and $X(\mathrm{Ca}) \approx X(\mathrm{Ti}) \approx 10^{-4}$ about 20,000 km $s^{-1}$. The abundance in the outermost layer in our spectral synthesis model has a marked similarity to this prediction. The characteristic velocity of the jet component in model 40A, assuming a non-relativistic jet, is lower than our dividing velocity between the main supernova ejecta and the high-velocity component ($v_{\mathrm{div}} \approx 55{,}000$ km $s^{-1}$); however, the dividing velocity is sensitive to the exact configuration. For the inner region, the same model predicts increasing mass fractions for Ca and Ti, reaching $X(\mathrm{Ca}) \approx 0.01$ along the jet axis and $X(\mathrm{Ca}) \approx 10^{-3}$ for the whole ejecta—an increase by a factor of 10 compared to the outer layer. This behaviour is again consistent with the spectrum-synthesis model result for SN 2017iuk, where we require more Ca and Ti in the lower-velocity material. This analysis therefore suggests that the composition structure is well represented by a configuration containing a jet and a cocoon. The jet-driven explosion also produces a flat density distribution, because it is represented by the continuously active central engine.

We reject the possibility that the ejecta extend further outwards in a smooth manner towards even higher velocities, because such material should create additional absorption at even higher velocities than we observed. Our rapid spectral observation and spectral modelling identify the outermost edge of the GRB-associated supernova ejecta, and such material would be hidden at later epochs without detectable traces.

## Data availability

The optical spectra obtained with GTC/OSIRIS and VLT/X-shooter are available in the GRBspec repository at http://grbspec.iaa.es. The optical spectra obtained with VLT/X-shooter are also available in the WISEREP repository at https://wiserep.weizmann.ac.il/object/7496. The optical data shown in the plots and tables and the Python codes used for the data analysis are available from the corresponding author on reasonable request. The entire photometric dataset is available at https://osf.io/apq3d/. Swift XRT and UVOT data are public (https://heasarc.gsfc.nasa.gov/docs/archive.html). The open-source code TARDIS used for the spectrum synthesis is available at https://tardis.readthedocs.io/en/latest/.


31. Gehrels, N. et al. The Swift gamma-ray burst mission. *Astrophys. J.* **611**, 1005–1020 (2004).
32. Greiner, J. et al. GROND – a 7-channel imager. *Publ. Astron. Soc. Pacif.* **120**, 405–424 (2008).
33. Roming, P. W. A. et al. The Swift ultra-violet/optical telescope. *Space Sci. Rev.* **120**, 95–142 (2005).
34. Poole, T. S. et al. Photometric calibration of the Swift ultraviolet/optical telescope. *Mon. Not. R. Astron. Soc.* **383**, 627–645 (2008).
35. Sari, R., Piran, T. & Narayan, R. Spectra and light curves of gamma-ray burst afterglows. *Astrophys. J.* **497**, L17–L20 (1998).
36. Šimon, V., Hudec, R., Pizzichini, G. & Masetti, N. Colors and luminosities of the optical afterglows of the gamma-ray bursts. *Astron. Astrophys.* **377**, 450–461 (2001).
37. Granot, J., Piran, T. & Sari, R. Images, light curves and spectra of GRB afterglow. *Astron. Astrophys. Suppl. Ser.* **138**, 541–542 (1999).
38. Arnaud, K. A. XSPEC: the first ten years. *ASP Conf. Ser.* **101**, 17–20 (1996).
39. Schady, P. et al. Dust and metal column densities in gamma-ray burst host galaxies. *Mon. Not. R. Astron. Soc.* **401**, 2773–2792 (2010).
40. Schlegel, D. J., Finkbeiner, D. P. & Davis, M. Maps of dust infrared emission for use in estimation of reddening and cosmic microwave background radiation foregrounds. *Astrophys. J.* **500**, 525–553 (1998).
41. Willingale, R., Starling, R. L. C., Beardmore, A. P., Tanvir, N. R. & O'Brien, P. T. Calibration of X-ray absorption in our Galaxy. *Mon. Not. R. Astron. Soc.* **431**, 394–404 (2013).
42. Cardelli, J. A., Clayton, G. C. & Mathis, J. S. The relationship between infrared, optical, and ultraviolet extinction. *Astrophys. J.* **345**, 245–256 (1989).
43. Pei, Y. C. Interstellar dust from the Milky Way to the Magellanic clouds. *Astrophys. J.* **395**, 130–139 (1992).
44. Poznanski, D., Prochaska, J. X. & Bloom, J. S. An empirical relation between sodium absorption and dust extinction. *Mon. Not. R. Astron. Soc.* **426**, 1465–1474 (2012).
45. Osterbrock, D. E. & Ferland, G. J. (eds) *Astrophysics of Gaseous Nebulae and Active Galactic Nuclei* (University Science Books, Sausalito, 2006).
46. Wilms, J., Allen, A. & McCray, R. On the absorption of X-rays in the interstellar medium. *Astrophys. J.* **542**, 914–924 (2000).
47. de Ugarte Postigo, A. et al. The luminous host galaxy, faint supernova and rapid afterglow rebrightening of GRB 100418A. Preprint at https://arxiv.org/abs/1807.04281 (2018).
48. Clocchiatti, A., Suntzeff, N. B., Covarrubias, R. & Candia, P. The ultimate light curve of SN 1998bw/GRB 980425. *Astron. J.* **141**, 163 (2011).
49. Ferrero, P. et al. The GRB 060218/SN 2006aj event in the context of other gamma-ray burst supernovae. *Astron. Astrophys.* **457**, 857–864 (2006).
50. Hjorth, J. The supernova-gamma-ray burst-jet connection. *Phil. Trans. R. Soc. Lond. A* **371**, 20120275 (2013).
51. Valenti, S. et al. The broad-lined type Ic supernova 2003jd. *Mon. Not. R. Astron. Soc.* **383**, 1485–1500 (2008).
52. Cano, Z. et al. GRB 161219B/SN 2016jca: a low-redshift gamma-ray burst supernova powered by radioactive heating. *Astron. Astrophys.* **605**, A107 (2017).
53. Dessart, J. A. et al. Radiative-transfer models for explosions from rotating and non-rotating single WC stars. Implications for SN 1998bw and LGRB/SNe. *Astron. Astrophys.* **603**, A51 (2017).
54. Nousek, L. et al. Evidence for a canonical gamma-ray burst afterglow light curve in the Swift XRT data. *Astrophys. J.* **642**, 389–400 (2006).
55. Perley, D. A., Schulze, S. & de Ugarte Postigo, A. GRB 171205A: ALMA observations. *GCN Circ.* 22252 (2017).
56. Patat, F. et al. The metamorphosis of SN 1998bw. *Astrophys. J.* **555**, 900–917 (2001).
57. Clocchiatti, A. et al. The type IC SN 1990B in NGC 4568. *Astrophys. J.* **553**, 886–896 (2001).

58. Mazzali, P. A. et al. The type Ic hypernova SN 2002ap. *Astrophys. J.* **572**, L61–L65 (2002).
59. Kerzendorf, W. E. & Sim, S. A. A spectral synthesis code for rapid modelling of supernovae. *Mon. Not. R. Astron. Soc.* **440**, 387–404 (2014).
60. Lucy, L. B. Nonthermal excitation of helium in type Ib supernovae. *Astrophys. J.* **383**, 308–313 (1991).
61. Mazzali, P. A., Iwamoto, K. & Nomoto, K. A spectroscopic analysis of the energetic type Ic hypernova SN 1997EF. *Astrophys. J.* **545**, 407–419 (2000).
62. Ashall, C. et al. GRB 161219B-SN 2016jca: a powerful stellar collapse. Preprint at https://arxiv.org/abs/1702.04339 (2017).
63. MacFadyen, A. I. & Woosley, S. E. Collapsars: gamma-ray bursts and explosions in "failed supernovae". *Astrophys. J.* **524**, 262–289 (1999).
64. Metzger, B. D. et al. The diversity of transients from magnetar birth in core collapse supernovae. *Mon. Not. R. Astron. Soc.* **454**, 3311–3316 (2015).
65. Hatano, K. et al. Ion signatures in supernova spectra. *Astrophys. J. Suppl. Ser.* **121**, 233–246 (1999).

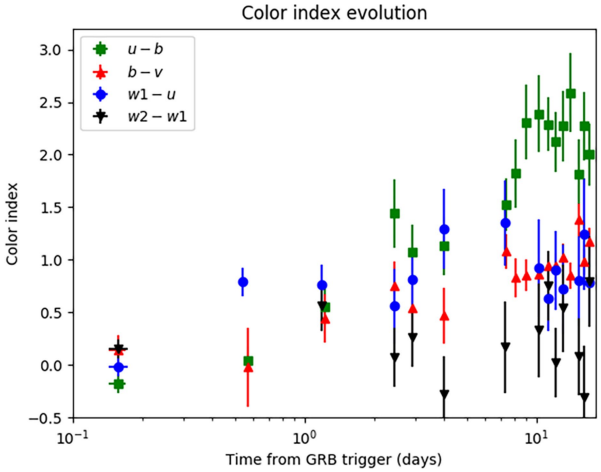


**Extended Data Fig. 1 | Early evolution of the colour index.** The evolution of the $u - b$, $b - v$, $uvw1 - u$ and $uvw2 - uvw1$ colour indices, computed from UVOT data in the first 18 days after the GRB trigger. Error bars represent 1 s.d.

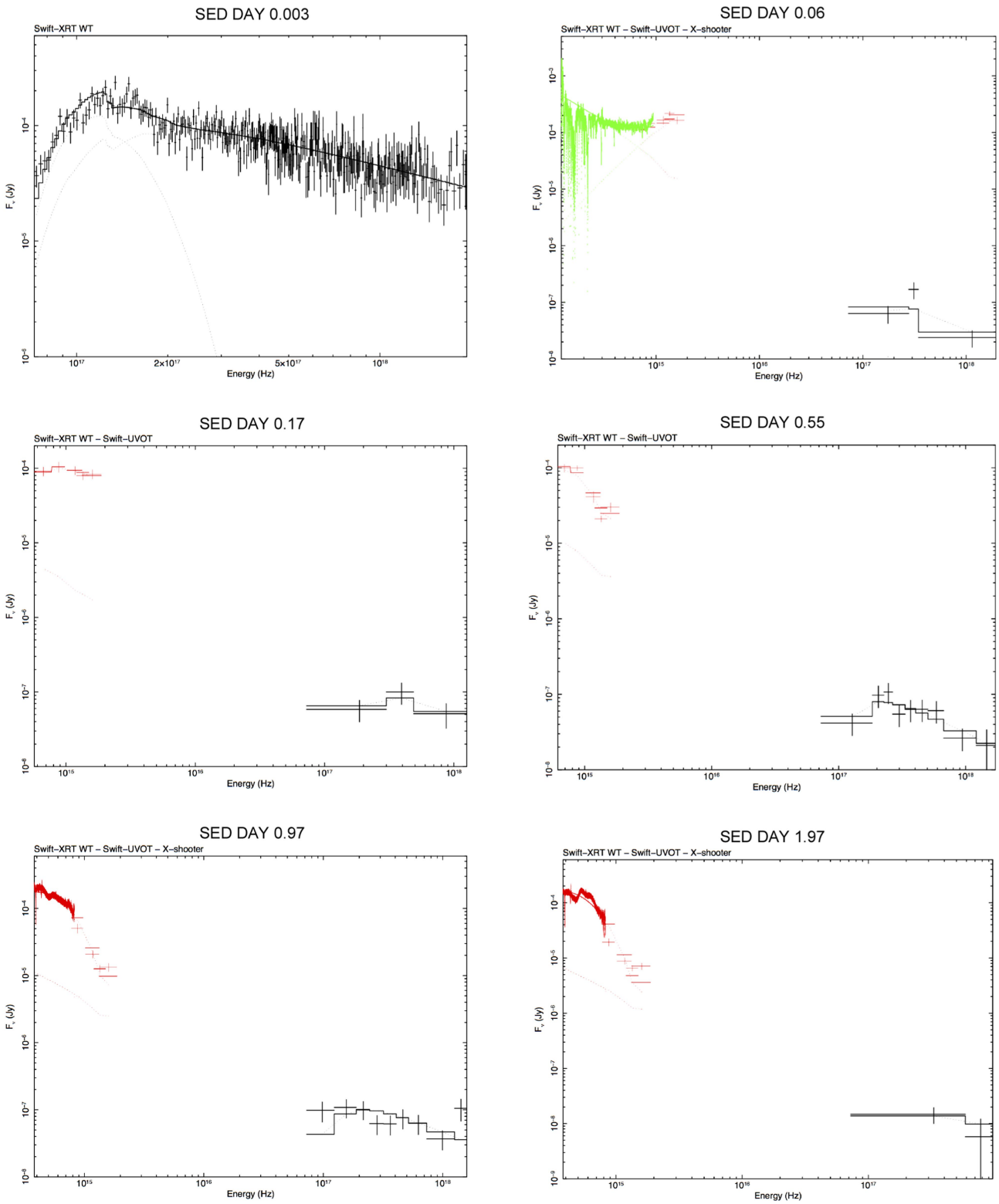


**Extended Data Fig. 2 | Modelling the SEDs.** SEDs for the epochs at $T_{SED1} = 0.003$ days and $T_{SED2} = 0.06$ days (top), $T_{SED3} = 0.17$ days and $T_{SED4} = 0.55$ days (middle), and $T_{SED5} = 0.97$ days and $T_{SED6} = 1.97$ days (bottom). All datasets use photometric data points obtained with Swift UVOT for the low-energy part of the spectrum (red). Error bars represent 1 s.d. Faint dotted lines represent the entire spectral model used, in flux density ($F_\nu$) units. The SED is complemented with VLT/X-shooter at day 0.06 (green) and GTC/OSIRIS spectra at day 0.97 and day 1.97 (red), whereas for the X-ray energy range we built specific Swift XRT spectra (black). An additional spectrum is shown in the top-left panel (black data) together with the best-fit results obtained for the Swift windowed-timing (WT) mode spectrum computed at 0.003 days using a black body plus power-law spectral model (solid line).

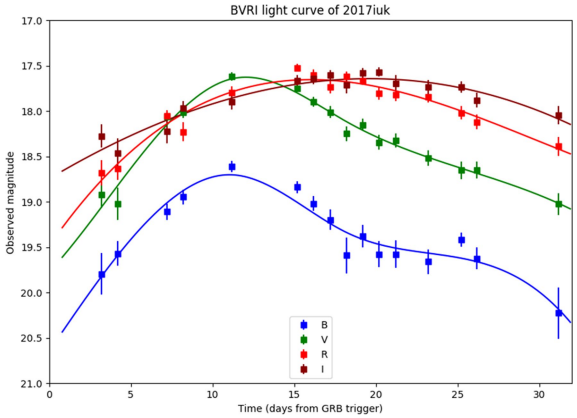


**Extended Data Fig. 3 | Evolution of the light curve of SN 2017iuk.** Evolution of the $BVR_CI_C$ magnitude of SN 2017iuk as observed with the RBT/PST2 telescope. Coloured curves represent the interpolation functions used to estimate the peak brightness. Error bars represent 1 s.d.

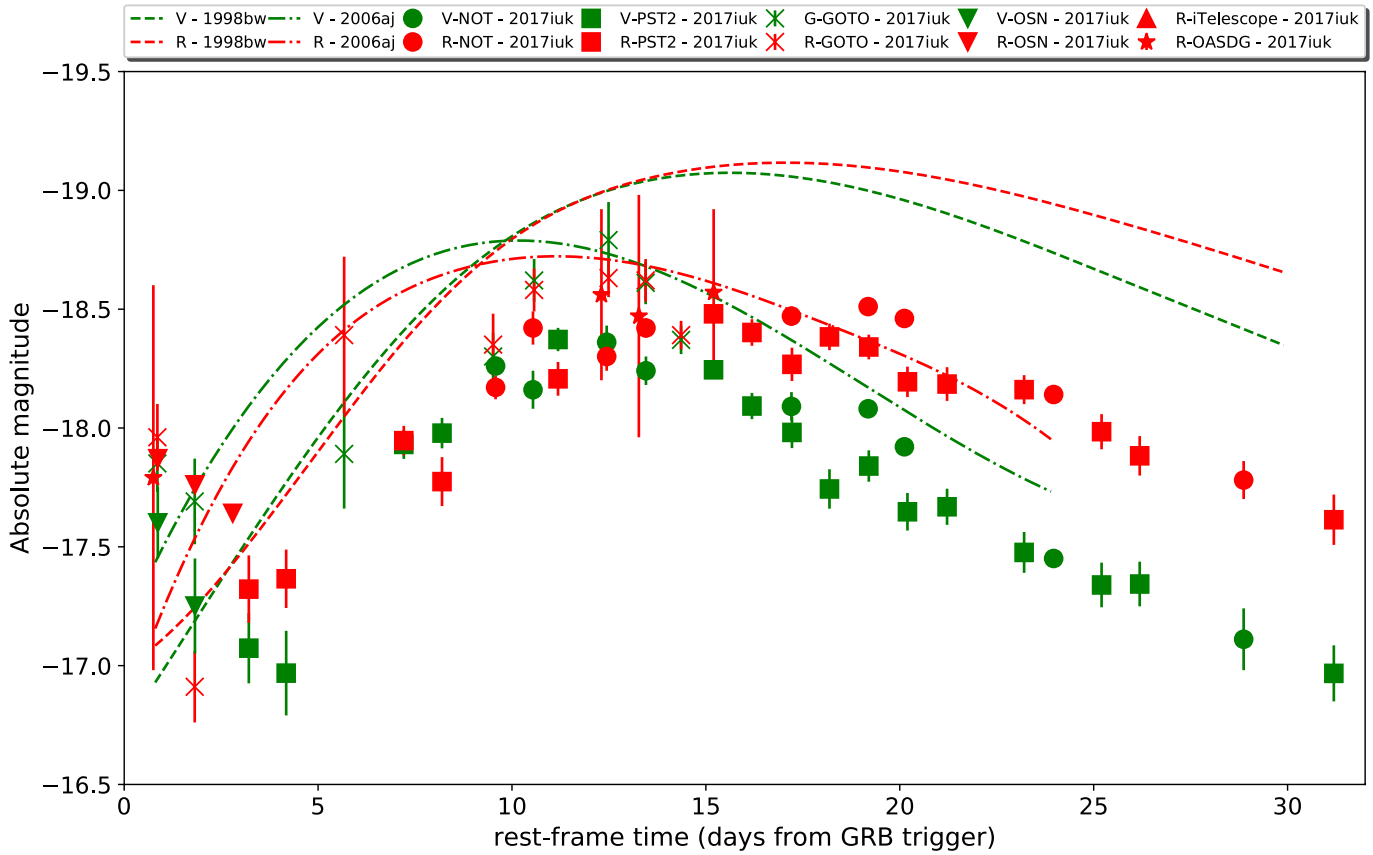


**Extended Data Fig. 4 | SN 2017iuk versus SN 1998bw and SN 2006aj.** Evolution of the $V$ (green) and $R_C$ (red) absolute magnitudes for SN 2017iuk (symbols), as observed from the NOT, OSN, RBT/PST2, GOTO and smaller telescopes (iTelescope, OASDG). The evolution in the first 30 days of SN 1998bw (dashed curves) and SN 2006aj (dot-dashed curves) are also shown, considering a common rest-frame time interval. Error bars represent 1 s.d.

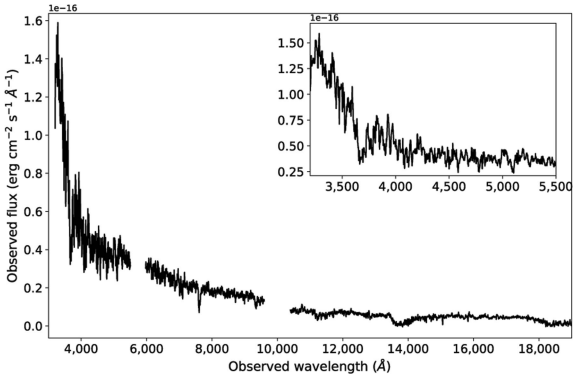


**Extended Data Fig. 5 | Spectrum of GRB 171205A/ SN 2017iuk obtained 1.5 h after the GRB detection.** This spectrum was obtained with VLT/X-shooter in the range 3,200–19,000 Å. The inset shows the UVB arm (3,200–5,500 Å), where the emission excess at wavelengths up to 4,000 Å and a possible absorption feature at about 3,700 Å are shown.

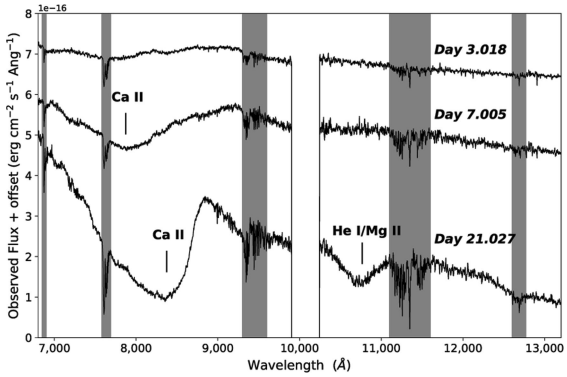


**Extended Data Fig. 6 | Spectroscopic evolution of SN 2017iuk in the NIR.** Grey regions indicate telluric features in the spectra. The possible He I $\lambda$10830/Mg II $\lambda$10914 feature is visible in the day-21 spectrum, while the Ca II triplet shows a P-Cygni profile at bluer wavelengths.

**Extended Data Table 1 | Log of the spectroscopic observations**

| Date | T - $T_0$ (days) | Time (UT) | Instrument | Exp. time (s) |
|---|---|---|---|---|
| 2017 12 05 | 0.0625 | 08:56:18 | X-shooter | 1x600 |
| 2017 12 06 | 0.975 | 06:44:42 | OSIRIS | 2x600 |
| 2017 12 07 | 1.947 | 06:05:03 | OSIRIS | 2x600 |
| 2017 12 09 | 3.018 | 07:46:23 | X-shooter | 2x400 |
| 2017 12 09 | 3.943 | 05:58:28 | OSIRIS | 5x600 |
| 2017 12 10 | 4.954 | 06:14:12 | OSIRIS | 3x600 |
| 2017 12 12 | 7.005 | 07:24:06 | X-shooter | 2x400 |
| 2017 12 13 | 7.982 | 06:54:38 | FORS | 1x600 |
| 2017 12 14 | 8.905 | 05:03:45 | OSIRIS | 3x600 |
| 2017 12 15 | 9.947 | 06:05:03 | OSIRIS | 3x600 |
| 2017 12 16 | 10.952 | 06:11:45 | OSIRIS | 2x400+2x400 |
| 2017 12 18 | 12.973 | 06:41:08 | OSIRIS | 2x300+2x600 |
| 2017 12 20 | 14.936 | 05:48:39 | OSIRIS | 2x300+2x500 |
| 2017 12 23 | 17.945 | 06:02:12 | OSIRIS | 2x300+2x500 |
| 2017 12 25 | 19.850 | 03:44:34 | OSIRIS | 2x300+2x500 |
| 2017 12 26 | 21.027 | 07:59:58 | X-shooter | 2x400 |
| 2018 01 01 | 26.861 | 04:00:38 | OSIRIS | 2x300+2x500 |
| 2018 01 04 | 29.926 | 05:34:52 | OSIRIS | 2x500+2x500 |

The values in the second column refer to days after the GRB discovery (at $T_0$). In the fifth column, the exposure times for the OSIRIS instrument refers to the R1000B grism if there is a single value and to the R1000B and R2500I grisms where there are two values.

**Extended Data Table 2 | Fit results of the SEDs built from GROND, Swift UVOT and XRT data**

| Epoch (days) | $\Gamma$ | $kT$ (eV) | $R_{BB}$ (cm) | $L_{BB}$ (erg s$^{-1}$) | $\chi^2/DOF$ |
|---|---|---|---|---|---|
| 0.003 | 1.65±0.03 | 86±5 | $(1.5\pm0.1)\times10^{12}$ | $(2.1\pm0.2)\times10^{45}$ | 904.7/765 |
| 0.06 | 2.07±0.22 | 7±4 | $(1.0\pm0.8)\times10^{13}$ | $(4.6\pm3.9)\times10^{42}$ | 710615.8/55388 |
| 0.17 | 1.65±0.39 | 1.3±0.8 | $(3.0\pm2.9)\times10^{14}$ | $(3.9\pm3.7)\times10^{42}$ | 138.0/31 |
| 0.55 | 1.83±0.19 | 0.9±0.4 | $(5.0\pm4.8)\times10^{14}$ | $(2.7\pm2.6)\times10^{42}$ | 76.3/75 |
| 1.04 | 1.77±0.15 | 0.6±0.1 | $(1.1\pm0.6)\times10^{15}$ | $(2.7\pm2.4)\times10^{42}$ | 3776.9/2128 |
| 2.01 | 1.88±0.60 | 0.5±0.1 | $(1.1\pm0.8)\times10^{15}$ | $(1.8\pm1.5)\times10^{42}$ | 10513.7/2063 |

DOF, degrees of freedom; $R_{BB}$, black-body emitting radius; $L_{BB}$, black-body emitted luminosity; $\Gamma$, photon index of the power-law spectral model.

**Extended Data Table 3 | Model parameters**

| $T - T_0$ (days) | $V_{ph}$ (km s$^{-1}$) | $T_{ph}$ (K) | $log(L_{bol}/L_{\odot})$ |
|---|---|---|---|
| 0.975 | 59,000 | 9,200 | 8.30 |
| 1.947 | 53,000 | 7,800 | 8.61 |
| 7.005 | 27,500 | 7,600 | 9.07 |
| 10.952 | 21,500 | 7,700 | 9.23 |
| 14.936 | 15,500 | 8,200 | 9.22 |

The photospheric velocity $V_{ph}$ (second column), the photospheric temperature $T_{ph}$ (third column) and the bolometric luminosity $L_{bol}$ in solar units (fourth column) are given for specific supernova epochs from the GRB trigger (first column).

**Extended Data Table 4 | Elemental abundances obtained from the synthesis model as a function of the expansion velocity**

| Elements | Velocity (km $s^{-1}$) | | | | |
|---|---|---|---|---|---|
| | $< 18,000$ | $18,000 - 25,000$ | $25,000 - 35,000$ | $35,000 - 55,000$ | $> 55,000$ |
| C | 1.0000E-02 | 1.0000E-02 | 1.0000E-02 | 1.0000E-02 | 1.0000E-02 |
| O | 8.9382E-01 | 9.0110E-01 | 9.0082E-01 | 9.3120E-01 | 8.8892E-01 |
| Mg | 5.0000E-02 | 5.0000E-02 | 5.0000E-02 | 5.0000E-02 | 5.0000E-02 |
| Si | 5.0000E-03 | 5.0000E-03 | 5.0000E-03 | 5.0000E-03 | 5.0000E-03 |
| S | 2.2000E-04 | 2.2000E-04 | 2.2000E-04 | 2.2000E-04 | 2.2000E-04 |
| Ca | 7.9077E-03 | 7.9077E-03 | 4.1576E-03 | 1.5326E-03 | 7.8265E-04 |
| Ti | 1.5765E-03 | 1.5765E-03 | 8.2654E-04 | 3.0154E-04 | 1.5154E-04 |
| Cr | 5.2594E-03 | 5.2594E-03 | 2.7594E-03 | 1.0094E-03 | 5.0935E-04 |
| Fe | 1.1870E-02 | 8.6700E-03 | 1.1870E-02 | 6.7000E-04 | 1.9870E-02 |
| Co | 2.8177E-04 | 2.0177E-04 | 2.8177E-04 | 1.7700E-06 | 4.8177E-04 |
| Ni | 1.4039E-02 | 1.0039E-02 | 1.4039E-02 | 3.8650E-05 | 2.4039E-02 |
| $^{56}$Ni | 5.6000E-02 | 4.0000E-02 | 5.6000E-02 | 0.0 | 9.6000E-02 |